13 June 2002

ELSEVIER

Chemical Physics Letters 359 (2002) 68–76

CHEMICAL PHYSICS LETTERS

www.elsevier.com/locate/cplett

Complex WS_2 nanostructures

R.L.D. Whitby [a], W.K. Hsu [a], T.H. Lee [a], C.B. Boothroyd [b], H.W. Kroto [a], D.R.M. Walton [a,*]

[a] *School of Chemistry, Physics and Environmental Science, University of Sussex, Falmer, Brighton BN1 9QJ, UK*
[b] *Department of Materials Science and Metallurgy, University of Cambridge, Pembroke Street, Cambridge CB2 3QZ, UK*

Received 11 February 2002; in final form 5 April 2002

Abstract

A range of elegant tubular and conical nanostructures has been created by template growth of $(WS_2)_n$ layers on the surfaces of single-walled carbon nanotube bundles. The structures exhibit remarkably perfect straight segments together with interesting complexities at the intersections, which are discussed here in detail in order to enhance understanding of the structural features governing tube growth. © 2002 Published by Elsevier Science B.V.

1. Introduction

Carbon nanotubes are essentially graphite sheets rolled into a cylinder, often with closed geodesic dome-shaped ends. The topologies of such tubes can usefully be described in terms of a lattice vector which defines tube chirality [1], an approach which also applies to more complex conical and helical nanostructures [2,3]. The folding of triple-layered MS_2 (M = Mo, W) lattices into closed structures is, however, more complicated than in the case of single sheet graphitic structures. The triple S–M–S layer is unable to form odd-membered rings (important in graphite curvature) because the W atoms can only bond to S [4]. This implies that 2D curved disinclinations may be rather difficult to achieve for MS_2 sheets and therefore closure may only occur in very limited circumstances. Margulis et al. [5] have proposed a model consisting of a rhombus, or triangular, apex surrounded by hexagons, in order to account for cusp structures of polyhedral MS_2 particles. However, these models are only valid in the context of localized curvature in MS_2 particles, i.e., the cusp structures [5,6]. In the work described here, a range of interesting complex WS_2 nanostructures (Figs. 1a–c), similar to those previously reported for mixed dichalcogenide nanostructures [7], has been investigated by high-resolution transmission electron microscopy (HRTEM).

2. Experimental

WS_2 nanostructures were produced by heating WO_3-coated single-walled carbon nanotube (SWCNs) bundles at 900 °C in the presence of a N_2/H_2S flow, as described elsewhere [8].

* Corresponding author. Fax: +44-1273-677196.
E-mail address: d.walton@sussex.ac.uk (D.R.M. Walton).

0009-2614/02/$ - see front matter © 2002 Published by Elsevier Science B.V.
PII: S0009-2614(02)00596-1

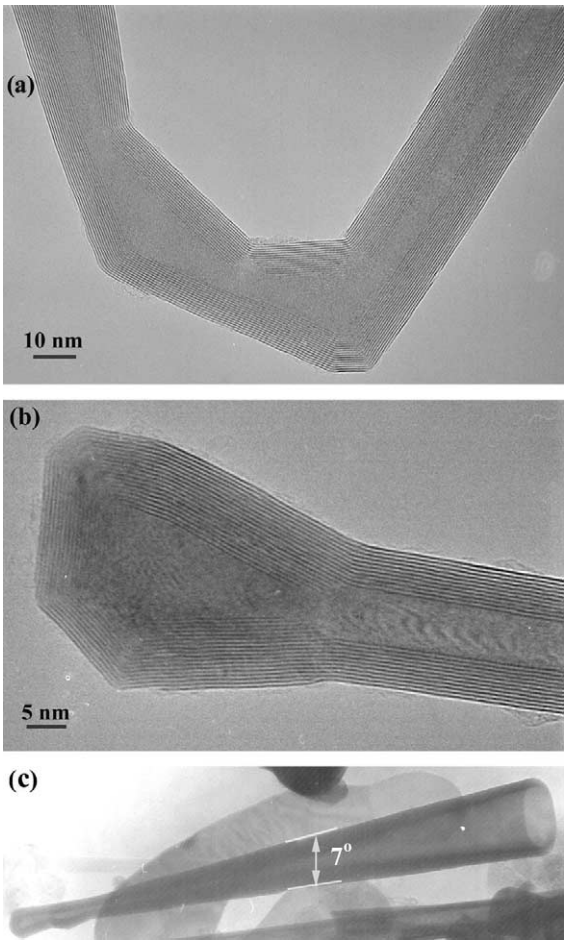

Fig. 1. HRTEM images of complex WS_2 nanostructures: (a) arm- like tube, (b) beaker-like capped tube, and (c) cone tube.

3. Results and discussion

HRTEM observations showed that all WS_2 nanostructures produced were hollow, i.e. no encapsulated WO_{3-x} particles were present. It has been shown that TEM beam energies, greater than 300 keV, induce the transformation of carbon nanotubes into onion-like carbon particles during 1 min [9]. In these experiments, WS_2 nanostructures were investigated using a JEOL-4000 EX at 400 keV and were found to be stable over time. No structural rearrangement took place during 1 h irradiation, thus allowing accurate defocusing studies to be carried out. Most SWCNs are damaged during the $WO_3 \rightarrow WS_2$ conversion process; a few remain encapsulated within the WS_2 nanotubes (see [8]).

Fig. 2a shows an HRTEM image of a complicated bent section of a WS_2 nanotube (Fig. 1a), which exhibits the following features: (a) variation of tube inner diameter from one section to the next; (b) lattice vacancies and layer discontinuities at the corners, and (c) only one apparently continuous WS_2 shell throughout the whole structure (layer 6). The evidence for claim (c) is as follows:

Fig. 2(a), A-side: The number of shells is reduced from 19 (right-hand section) to 13 (left-hand section). Shells 1–4 and 10–19 terminate before the first bend (arrows 5–9), and shells 5 and 8 terminate before the second bend (arrows 6–9, respectively). Only shells 6, 7 and 9 appear to be continuous on the A-side.

Fig. 2a, B-side: Before the first bend, shells 1–2 and 7–19 are discontinuous and terminate at the numbered curves. Only shells 3–6 appear to be continuous throughout the B-side. It is noteworthy that shells 3 and 4, which terminate before the first bend (arrows), reappear after the second and third bends, respectively (A-side, arrows 3′ and 4′). Shell 2 may contain a large lattice vacancy, which reappears on the B-side before the first bend (arrow 2′, also see insert, Fig. 2a).

From these observations (based on Fig. 2b) it appears that only shell 6 (Fig. 2b) may be complete (Fig. 2b). The A-side exhibits positively curve bends (i.e., K_1, K_2 and K_3, Fig. 2b), in contrast to the B-side, which exhibits negative curved ones (i.e., K_4, K_5 and K_6, Fig. 2b). The triangular and rhombic apex models [5,6] do not fit structures K_1–K_6, because they are not cusps, but arise as a result of WS_2 layer bending. The main feature of bent layers is that the d-spacing remains unchanged. In cusped structures the variation in d-spacing can be observed by HRTEM [10]. Fig. 2a exhibits a constant d-spacing through the bending.

2D curvature in a graphene sheet requires the presence of non-hexagonal rings, e.g., 5- and 7-membered rings [11]. The complex WS_2 2D curvature involves the presence of various lattice defects. Shell 6 is divided into seven sections (from right to left, Fig. 2c), in order to consider the geometry of the WS_2 nanostructure. Section 1 is

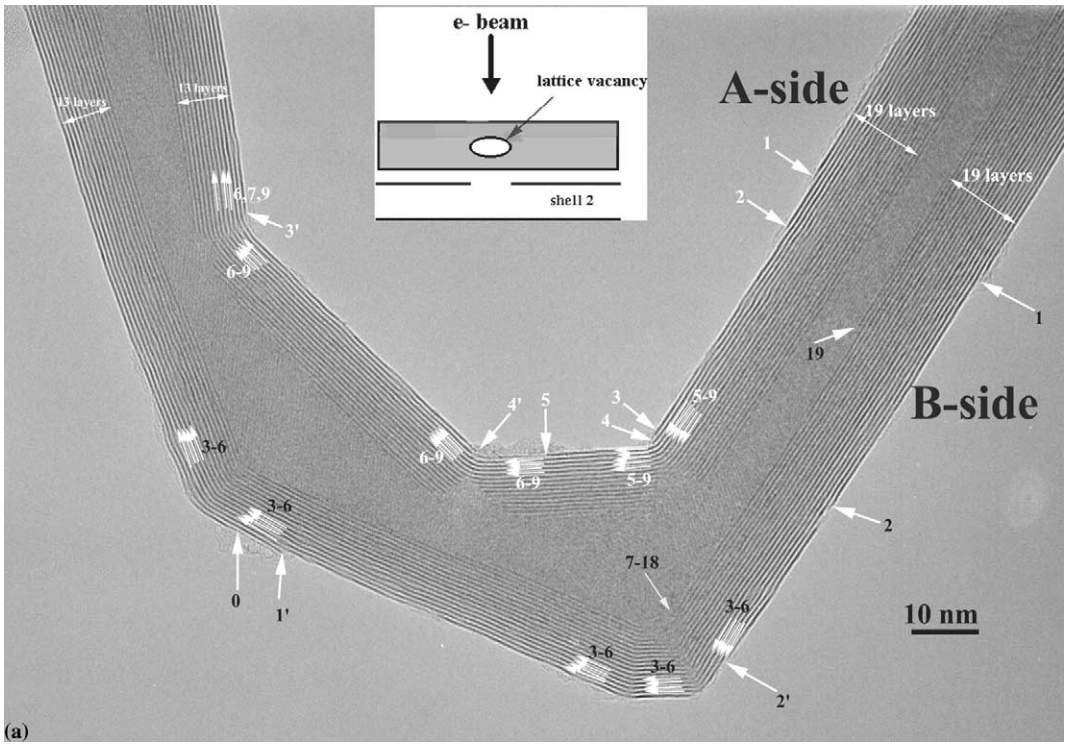

Fig. 2. (a) Enlarged HRTEM image of Fig. 1a. Inset: the structure of shell 2; (b) The geometry of isolated shell 6 from Fig. 2a. The shell can be divided into seven sections; section 1 is cylindrical and sections 2–7 are conical; (c) Individual conical components 1–7. The sizes are based on Fig. 2a. The left panel shows the unfolded cone 2, which exhibits a curved corner at its apex; (d) A bent carbon nanotube. The helicity varies from one side to the other; (e) Lattice re-matching processes along two connecting edges (see text).

cylindrical, whereas sections 2–7 are conical. The adjacent sections have the same diameter at the interface (bend), which allows continuous extension of WS_2 hexagonal rows from one section to the next. In order to maintain the triple-layered S–W–S configuration at the bend, the atom types between two connecting edges must be different: e.g. W atoms on the section 1 edge and S atoms on the section 2 edge, and vice versa. In carbon nanotubes, the presence of 5- and 7-membered rings induces tube bending, resulting in the variation of helicity from one tube section to another (Fig. 2d). This phenomenon arises because the presence of a pentagon in a hexagonal network gives rise to positive curvature, whereas a heptagon results in negative curvature. Accordingly, hexagonal rows may terminate (or start) at the pentagon (or at the heptagon) [12] and the tube helicity will change at the bending junction. The apparently intact shell 6 (Fig. 2b) implies that WS_2 hexagon rows extend continuously from section to section. Because only section 1 is perfectly cylindrical, the arrangement of hexagonal rows along the tube axis in conical sections may not remain the same as in section 1. In other words, the conical sections would have individual patterns constructed from hexagonal rows, i.e. the helicity varies from section to section.

In order to study the connections between the various segments, individual cones were measured (Fig. 2c) and unfolded into 2D structures, followed by mapping unfolded structures on a hexagonal WS_2 lattice. We find that lattice mismatches are present along the connecting edges of two unfolded cones. The lattice misfits certainly arise from the difficulty in satisfying complex cusp structures in a triple WS_2-layered structure. This implies that dislocations are inevitable at the junctions between two cones. However, slight

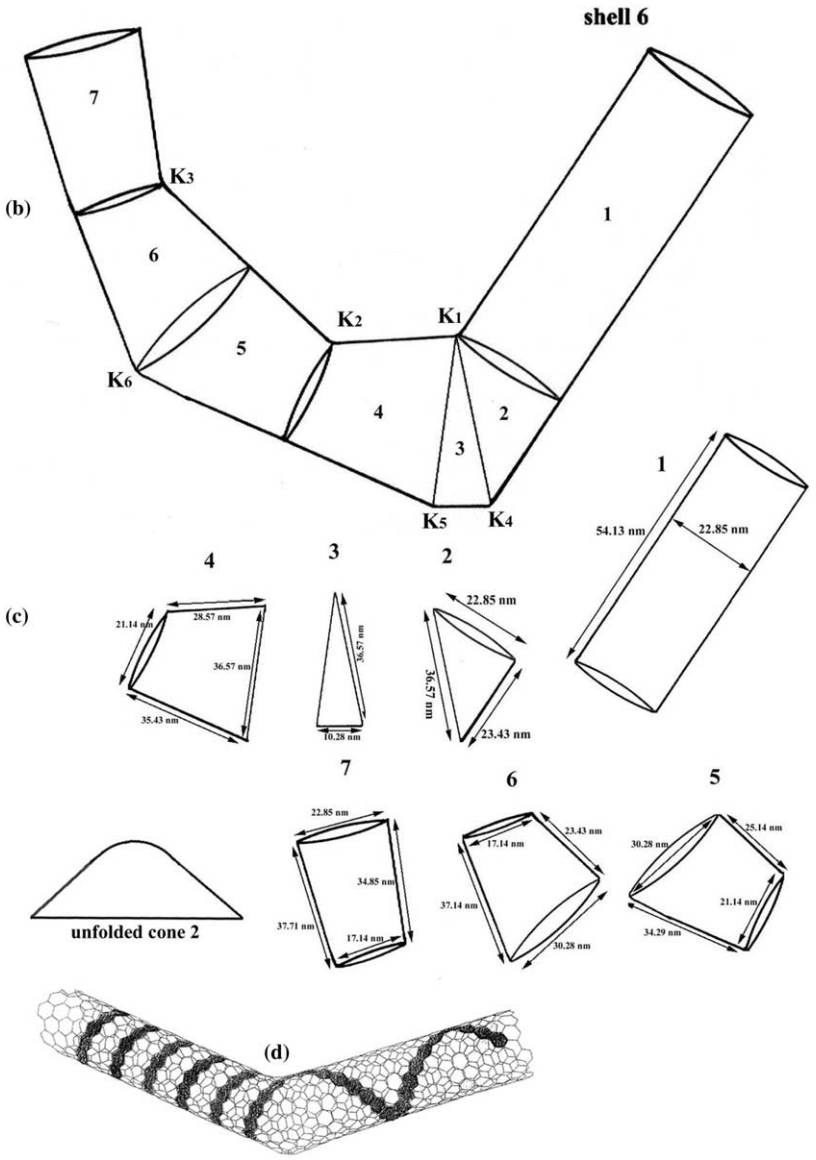

Fig. 2. *(continued)*

translation of the lattice along the connecting interface, until W atoms are paired with S atoms (B–B′, Fig. 2e), may accommodate this mismatch to some extent. The introduction of additional hexagonal rows (C–C′, Fig. 2e), or leaving unconnected lattices as vacancies (A, Fig. 2e) between connecting edges, probably also occurs. For example, the mismatched lattices can be re-matched by a 2.7 Å translation of section 2 (B–B′, Fig. 2e); 2.7 Å corresponds to the distance between adjacent W atoms along the zigzag edge [13]. Alternatively, insertion of an additional WS_2 hexagonal row between sections 1 and 2 (C, Fig. 2e) can also re-match the triple-layered S–W–S lattice (C′, Fig. 2e). We find that lattice re-matching is valid only for connecting the unfolded cylinder 1 and the

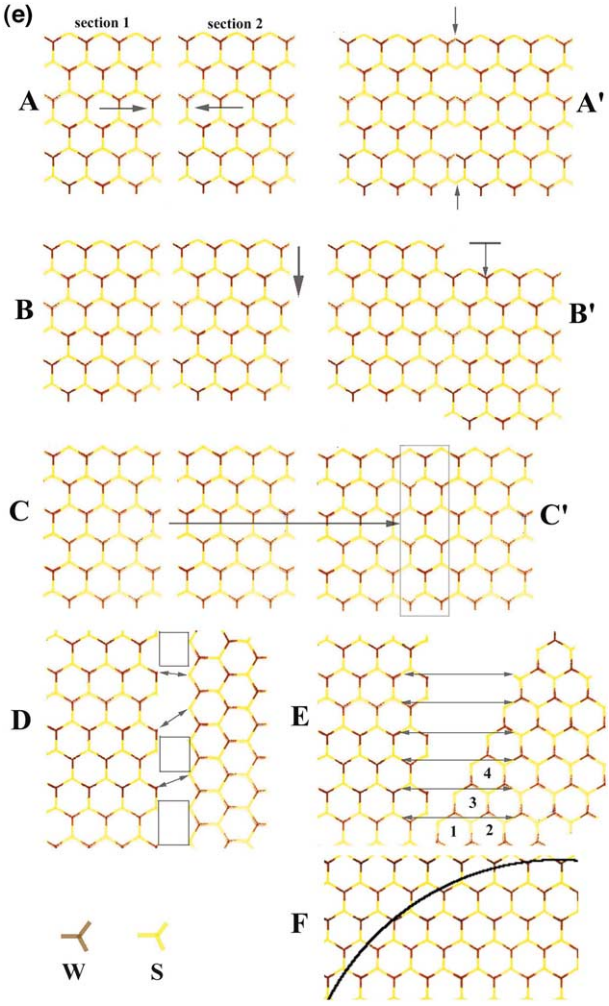

Fig. 2. *(continued)*

unfolded cone 2, because their edges are essentially linear. The edges of unfolded cones 2–7 are not linear, but curved. For example, the unfolded cone 2 is triangular, however its apex is curved (Fig. 2c). Various curves are present along the edges of unfolded cones 3–7, which makes lattice mapping difficult. For example, mapping a curve on a WS_2 lattice frequently results in an unsymmetrical division of a W–S bond (F, Fig. 2e), which means that the adjacent connecting edges would require an excess of W and S atoms in order to re-establish S–W–S bond configuration. The re-establishment of S–W–S bonds is displayed in (E, Fig. 2e); here the elimination of atoms (along the armchair edge, left section) and of hexagons 1–4 (along the zigzag edges, right section) is required in order to reconstruct S–W–S bonds (arrows, E, Fig. 2e). However, if the re-establishment of S–W–S bonds can only be achieved locally along the connecting edges (arrows, D, Fig. 2e), the unconnected edge lattices will remain as vacancies (e.g. squares, etc., D, Fig. 2e).

The excess of W and S atoms (C–C′, Fig. 2e) and a minor lattice translation (B–B′, Fig. 2e) can be accommodated via WS_2 sheet flexibility along the in-plane direction, due to a concertina-like

structure [14]. Because shell 6 is complete, lattice translation (C–C′, Fig. 2e) and hexagon insertion (B–B′, Fig. 2e) are likely to be present at the bends. It is noteworthy that shell 6 weaves slightly along the in-plane direction (Fig. 2a). In fact, layer weaving can also be found in straight WS_2 nanotubes. A typical example is shown in Fig. 3a, the weaving layers being highlighted within the white square. However, the mean value of separation across layers is maintained (6.2 Å). Fig. 3b provides an example of another WS_2 nanotube which contains nine shells and is almost defect-free with minimal localized interweaving (white squares). It is likely that the excess of atoms (or hexagonal rows) and the lattice translations along the connecting edges will produce stress along the in-plane direction, as exemplified by shell 6 (Fig. 2a). In fact, the excess of hexagons (or W and S atoms) is essential in a defect-free multi-walled nanotube, because a constant layer separation along the c-axis can only be maintained when the number of hexagons in each shell is not identical [15]. The excess of atoms can be accommodated either by extending the layer into a tube cap [16] or by interweaving, i.e., interfacial dislocation [17].

The bulb-ended WS_2 nanotube (Fig. 1b), also consists of discontinuous layers (white arrows 1 and 2, Fig. 4a), lattice vacancies (white squares 1 and 2, Fig. 4a) and interwoven layers (white square 3, Fig. 4a). A layer branched structure is

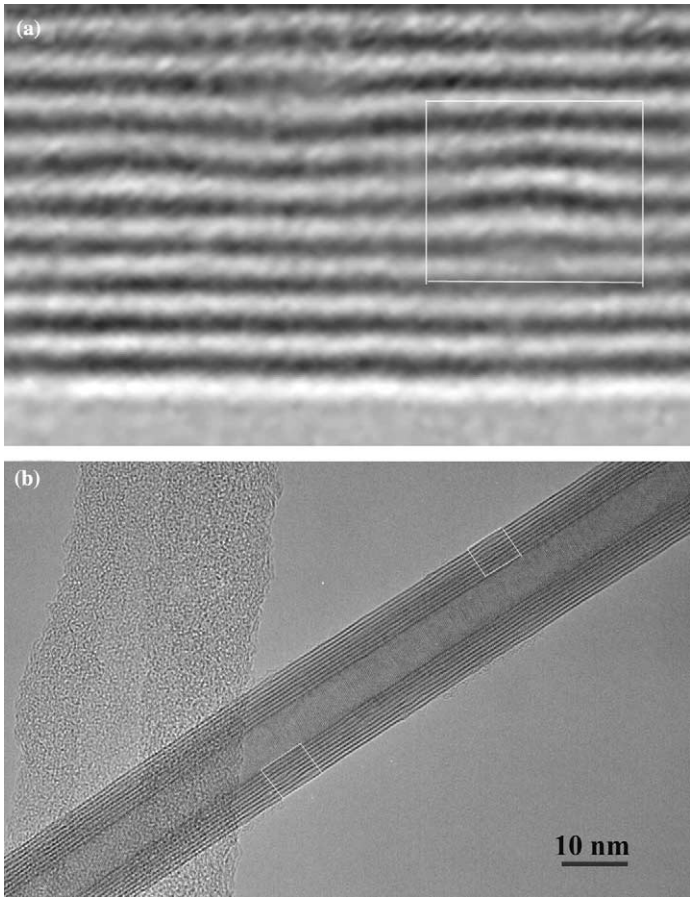

Fig. 3. (a) An enlarged-HRTEM image of a layer weaving structure (square) from a straight WS_2 nanotube.; (b) Layer weaving structures (squares) in a straight WS_2 nanotube.

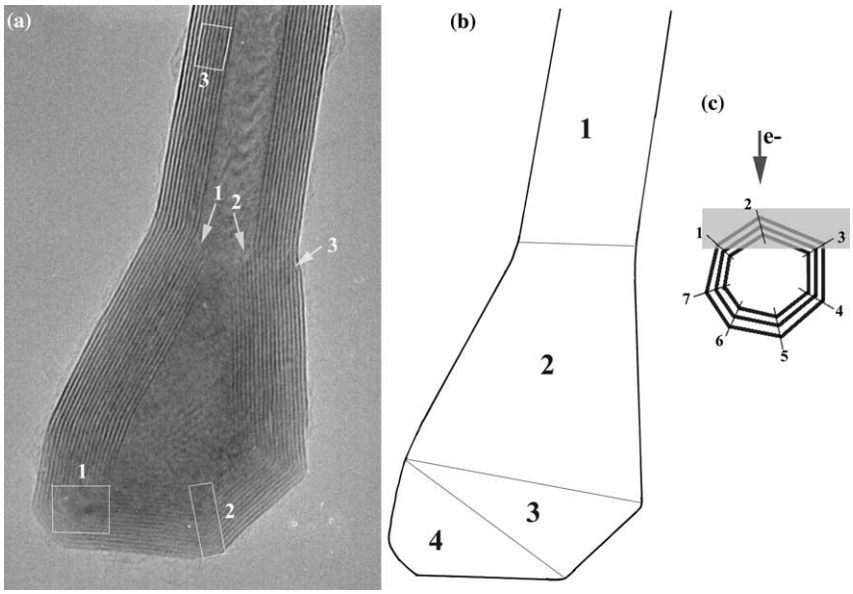

Fig. 4. (a) Enlarged HRTEM image of a beaker-like capped WS_2 nanotube (Fig. 1b). Arrows 1 and 2: discontinuous layers. Arrow 3: layer branching structure. Squares 1 and 2: obscured layer fringes at cusps 1 and 2. Square 3: weaving layers (see text); (b) The beaker-like nanotube divided into four sections. Sections 1 and 2 are cylindrical and conical, respectively. Sections 3 and 4 are asymmetric polyhedra. (c) An asymmetrical polyhedral particle vertical to the TEM beam; grey band: defocus depth (see text).

also present (arrow 3, Fig. 4a). Layer branching has been discussed previously and it was proposed that the absence of a W atom in the hexagonal lattice causes the top and lower S layers to split [18]. Fig. 4a can also be divided into four sections (Fig. 4b), however we were unable to depict an accurate 3D geometry for the bulb nanotube via tilting within TEM, because the layered fringes, particularly for sections 3 and 4, were obscured significantly. Note: the obscured layer fringes are mostly present in the cusp regions (e.g., white squares 1 and 2, Fig. 4a) and are also found in polyhedral carbon nanoparticles [19]. The nanotube structure does not show obscured fringes when the tube walls are located within the defocus depth, because the tube walls are always aligned with the TEM beam. However at the cusps, the walls are not generally aligned with the beam. For example, an asymmetric polyhedral particle (Fig. 4c) will only result in clear layer fringes at cusp 2, because only cusp 2 is located within the defocus depth (grey band, Fig. 4c). In Fig. 4a, the outermost layer fringe is still visible (square 1) and the fringes gradually fade from the second layer. A similar fringe also disappears from square 2 (Fig. 4a). The visible fringes are similar to cusps 1 and 3 (Fig. 4c), in which only outer layers are located within the defocus depth. Square 4 (Fig. 4a) exhibits relatively strong layer fringes, corresponding to cusp 2 (Fig. 4c). The presence of obscured fringes in Fig. 4a (squares 1 and 2) implies that sections 3 and 4 (Fig. 4b) are polyhedral; clearly sections 1 and 2 are cylindrical and conical, respectively. Meanwhile, due to obscured fringes, the layer continuity in the cusp regions (i.e. squares 1 and 2) remains unclear.

Fig. 1c shows a conical WS_2 structure. The cone angle is ca. 7°, open at the wide end and closed by a complicated set of cavities at the narrow end (Figs. 5a,c). The open end appears to exhibit an elliptical pattern indicating that it is more or less round (Fig. 5a). The central line of the cone is ca. 3.5° tilted away from the horizontal (Fig. 5b) and the ellipse projection results from the line A and B (Fig. 5b). The rim of the oval cone base appears to be fairly regular (Fig. 5a) and bisection of the ellipse (line c–d, Fig. 5a) is symmetric.

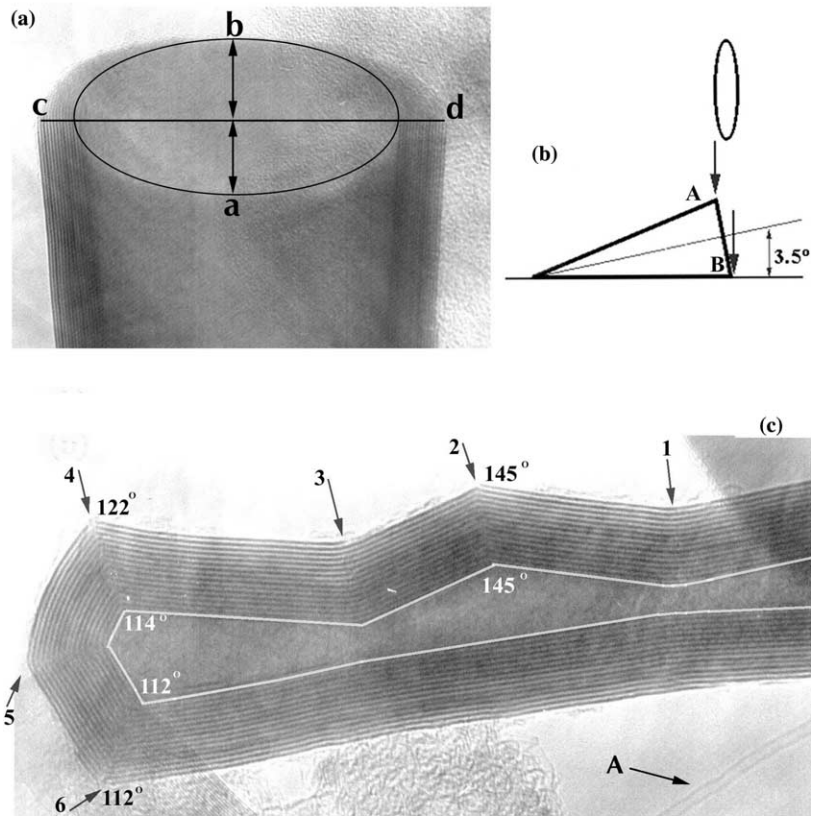

Fig. 5. (a) An enlarged HRTEM image of a cone base (Fig. 1c); (b) Projection from a symmetrical cone base; (c) An enlarged HRTEM image of the tube tip (Fig. 1c), a SWCN is also observed (arrow A).

The cone tube (Fig. 1c) exhibits complex cavities near the tip region (Fig. 5c). In particular, a 145° hump-like structure (arrows 1–2–3, Fig. 5c) is present on one side of the tube (arrows 4–6). Analogous humps have been observed in carbon nanotubes where it is conjectured that the combinations of 5- and 7-membered rings are involved [20]. Although, in Fig. 5c, the outermost layer of the cone appears to be discontinuous, the layers below the outermost one and between the cusps seem to be continuous, i.e., section 1 (arrow 1–2, Fig. 5c), section 2 (arrow 2–3), section 3 (arrow 3–4), section 4 (arrow 4–5) and section 5 (arrow 5–6). Again, layer fringes are obscured, suggesting that dislocations are present at cusps 5 and 6 along the c-axis, (cusps 2 and 4 show layer bending, as indicated by relatively clear layer fringes). The saddle-like curves (arrows 1 and 3), due to layer bending, exhibit well-defined layered fringes and the mean value of layer separation across the bending layers remains: 6.2 Å. We find that the cusp angles measured at the outermost layer differ slightly from the value obtained for the innermost layer (inner outline, Fig. 4d). For example, the angles of the outer- and inner-layers for cusps 4 and 6 are ca. 122°, 114°, and 112° and 112°, respectively. Cusp 2 exhibits the same angle for both outer- and inner-layers (ca. 145°). The overall angles of cusps 4 and 6 however approximate to the value reported by Margulis et al. [5], i.e. the WS_2 rhombus apex. Thus cusps 3 and 4, 4 and 5, and 5 and 6 may be connected via the structure involving the rhombus apex model, and lattice re-matching (Fig. 2e) may not be necessary. The geometry between sections 1 (arrow 1–2) and 2 (arrow 2–3) is conical, similar to sections 5 and 6 (Fig. 2b). Ac-

cordingly, the connection between sections 1 and 2 requires lattice re- matching.

4. Conclusion

We used Cerius-2 software in conjunction with HRTEM to investigate the origin of localized curvatures. However, the modeling is usually limited to a few thousand atoms and is not readily applicable to the present structures, which involve tens of thousands of atoms, e.g., nanotubes and bucky- onions. For example, previous workers smoothed the facets of giant icosahedral fullerenes (i.e., C_{540}, C_{960} and C_{1500}) by introducing heptagonal as well as pentagonal rings into the carbon network [21] (bucky-onion structure) [9]. However, such structures, generated via a high-energy electron beam (i.e. atom knock-on effect, 300–400 keV, duration 30–60 s), are unstable, because further irradiation tends to destroy them [9]. Furthermore, lattice defects (i.e., vacancies) are present in onion structures [9]. In fact, the presence of lattice vacancies is essential for onion formation. Sakar [22] has discussed a model, consisting of defective giant fullerenes, which, to some extent, approximates to the onion structure. In this Letter, we show that the presence of variously curved nanostructures mainly arises from lattice imperfections (vacancies, discontinuous layers and layer bending) and not from geometric bonding anomalies.

Acknowledgements

We thank the Leverhulme Trust, Royal Society and Wolfson Foundation for financial support.

References

[1] D.H. Robertson, D.W. Brenner, J.W. Mintmire, Phys. Rev. B 45 (1992) 12592.
[2] A.T. Balaban, D.J. Klein, X. Liu, Carbon 32 (1994) 357.
[3] K. Akagi, R. Tamura, M. Tsukada, S. Itoh, S. Ihara, Phys. Rev. Lett. 74 (1995) 2307.
[4] W.K. Hsu, Y.Q. Zhu, N. Yao, S. Firth, R.J.H. Clark, H.W. Kroto, D.R.M. Walton, Adv. Funct. Mater. 11 (2001) 69.
[5] L. Margulis, G. Salitra, R. Tenne, M. Talianker, Nature 365 (1993) 113.
[6] P.A. Parilla, A.C. Dillon, K.M. Jones, G. Riker, D.L. Schulz, D.S. Ginley, M.J. Heben, Nature 397 (1999) 114.
[7] M. Nath, K. Mukhopadhyay, C.N.R. Rao, Chem. Phys. Lett. 352 (2002) 163.
[8] R.L.D. Whitby, W.K. Hsu, C.B. Boothroyd, P.C.P. Watts, H.W. Kroto, D.R.M. Walton, Appl. Phys. Lett. 79 (2001) 4574.
[9] D. Ugarte, Nature 359 (1992) 707.
[10] D.J. Srolovitz, S.A. Safran, M. Homyonfer, R. Tenne, Phys. Rev. Lett. 74 (1995) 1779.
[11] A. Fonseca, K. Hernadi, J.B. Nagy, P. Lambin, A.A. Lucas, Carbon 33 (1995) 1759.
[12] S. Iijima, Nature 354 (1991) 56.
[13] R.L.D. Whitby, W.K. Hsu, C.B. Boothroyd, P.K. Fearon, H.W. Kroto, D.R.M. Walton, Chem. Phys. Chem. 2 (2001) 620.
[14] W.K. Hsu, B.H. Chang, Y.Q. Zhu, W.Q. Han, H. Terrones, M. Terrones, N. Grobert, A.K. Cheetham, H.W. Kroto, D.R.M. Walton, J. Am. Chem. Soc. 122 (2000) 10155.
[15] W.K. Hsu, S. Firth, P. Redlich, M. Terrones, H. Terrones, Y.Q. Zhu, N. Grobert, A. Schilder, R.J.H. Clark, H.W. Kroto, D.R.M. Walton, J. Mater. Chem. 10 (2000) 1425.
[16] G.B. Adams, O.F. Sankey, J.B. Page, M. Okeeffe, D.A. Drabold, Science 256 (1992) 1792.
[17] X.F. Zhang, X.B. Zhang, G. Vantendeloo, S. Amelinckx, M.O. Debeeck, J. Vanlanduyt, J. Cryst. Growth 130 (1993) 368.
[18] W.K. Hsu, Y.Q. Zhu, S. Firth, M. Terrones, H. Terrones, S. Trasobares, R.J.H. Clark, H.W. Kroto, D.R.M. Walton, Carbon 39 (2001) 1107.
[19] P.M. Ajayan, T. Ichihashi, S. Iijima, Chem. Phys. Lett. 202 (1993) 384.
[20] S. Iijima, Mater. Sci. Eng. B-Solid State Mater. Adv. Technol. 19 (1993) 172.
[21] K.R. Bates, G.E. Scuseria, Theor. Chem. Acc. 99 (1998) 29.
[22] A.K. Sakar, Ph.D dissertation, University of Sussex, 1994, p. 114.